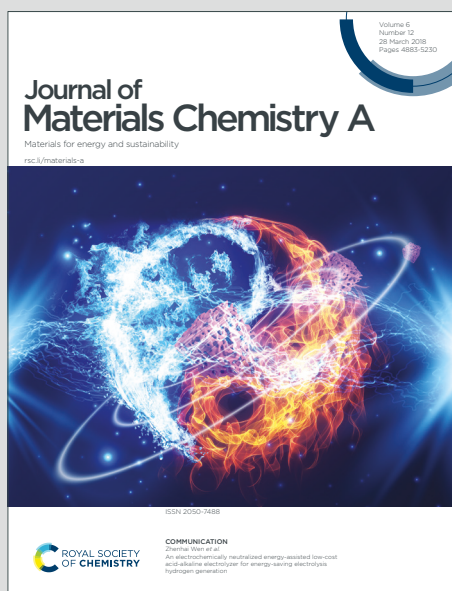


# Journal of Materials Chemistry A

Materials for energy and sustainability

Accepted Manuscript

This article can be cited before page numbers have been issued, to do this please use: A. Taufik, A. Yoko, C. Han, W. Wahyudiono, S. Ohara and T. Adschiri, *J. Mater. Chem. A*, 2026, DOI: 10.1039/D5TA07868G.



This is an Accepted Manuscript, which has been through the Royal Society of Chemistry peer review process and has been accepted for publication.

Accepted Manuscripts are published online shortly after acceptance, before technical editing, formatting and proof reading. Using this free service, authors can make their results available to the community, in citable form, before we publish the edited article. We will replace this Accepted Manuscript with the edited and formatted Advance Article as soon as it is available.

You can find more information about Accepted Manuscripts in the [Information for Authors](#).

Please note that technical editing may introduce minor changes to the text and/or graphics, which may alter content. The journal's standard [Terms & Conditions](#) and the [Ethical guidelines](#) still apply. In no event shall the Royal Society of Chemistry be held responsible for any errors or omissions in this Accepted Manuscript or any consequences arising from the use of any information it contains.

# *In Situ* Photo-Fenton-like Reaction and Oxygen Evolution through Polaron-Mediated WO<sub>3</sub>

*Ardiansyah Taufik*<sup>1,\*</sup>, *Akira Yoko*<sup>1,2,\*</sup>, *Chunli Han*<sup>1</sup>, *Wahyudiono*<sup>3</sup>, *Satoshi Ohara*<sup>4</sup>, *Tadafumi*

*Adschiri*<sup>1,4,\*</sup>

<sup>1</sup>WPI – Advanced Institute for Materials Research (WPI-AIMR), Tohoku University, 2-1-1

Katahira, Aoba-ku, Sendai, Miyagi 980-8577, Japan

<sup>2</sup>International Center for Synchrotron Radiation Innovation Smart (SRIS), Tohoku University,

Aramaki Aza-Aoba, Aoba-ku, Sendai, 980-8572, Japan

<sup>3</sup>Department of Chemical Engineering, Institut Teknologi Sepuluh Nopember, Kampus ITS

Sukolilo, Surabaya, 60111, Indonesia

<sup>4</sup>New Industry Creation Hatchery Center, Tohoku University, Sendai 980-8579, Japan

**KEYWORDS:** Photo Fenton-like; polaron; strain; electron localization; WO<sub>3</sub>

**ABSTRACT.** The effective utilization of both electrons and holes in semiconductor-based photocatalysis is crucial for enhancing light-driven chemical reactions. However, the photocatalytic performance of WO<sub>3</sub> is limited by its low conduction band potential, which restricts its ability to generate reactive species such as superoxide radicals and to facilitate hydrogen production. Consequently, WO<sub>3</sub> primarily relies on holes for redox processes, reducing its overall photocatalytic efficiency. This paper proposes a novel strategy to simultaneously exploit both



charge carriers by activating a photo-Fenton-like reaction driven by polaronic phenomena of electrons ( $W^{5+}$  formation). Electrons are responsible for generating hydroxyl radicals ( $\bullet OH$ ), enabling the degradation of Acid Orange 7 dye with an activity ten times higher than that of the conventional Fenton reaction. Meanwhile, holes effectively drive the oxygen evolution reaction (OER), achieving an oxygen yield of  $1.62 \text{ mmol g}^{-1} \text{ h}^{-1}$ . The polaronic behaviour of  $WO_3$  was further optimized by accelerated supersaturation process through protonation which enhances the surface properties and increase  $W^{5+}$  formation during light irradiation. This strategy led to approximately threefold enhancement in Acid Orange 7 degradation and a 2.3-fold increase in OER performance ( $3.66 \text{ mmol g}^{-1} \text{ h}^{-1}$ , one of the highest reported values). Overall, this study presents a new approach to optimizing charge carrier utilization in photocatalysis, offering a promising pathway toward more efficient and versatile semiconductor-based systems.

## 1. INTRODUCTION

The photo-Fenton reaction has emerged as a promising solution for wastewater treatment due to its strong oxidative capability in decomposing a wide range of pollutants<sup>1</sup>, including synthetic dyes<sup>2,3</sup>, pharmaceuticals,<sup>4</sup> and radioactive waste<sup>5</sup>. This process involves the reaction of iron salts with hydrogen peroxide, generating highly reactive hydroxyl radicals ( $\bullet OH$ ) that act as powerful oxidizing agents. However, the practical application of the Fenton reaction faces a major limitation: the residual iron salts remain in the solution after the reaction and are difficult to recover, potentially causing secondary pollution in water sources.<sup>6</sup> To address this issue, researchers have explored immobilizing iron sources in the form of iron oxides/hydroxides or anchoring them onto various supports such as metal oxide semiconductors<sup>7,8</sup>, metal–organic



frameworks (MOFs)<sup>9</sup>, and carbon-based materials<sup>10</sup>. Despite these advances, iron leaching—particularly under acidic conditions—remains a significant challenge,<sup>11,12</sup> limiting the long-term stability and sustainability of the process.

Instead of focusing solely on stabilizing iron ions, a more promising strategy is to develop stable materials that can generate hydroxyl radicals ( $\bullet\text{OH}$ ) through interactions with  $\text{H}_2\text{O}_2$ . For instance, previous studies have reported that  $\text{TiO}_2$  with a high concentration of  $\text{Ti}^{3+}$  defects can serve as effective candidates. However, these  $\text{Ti}^{3+}$  defect sites are not reversible, leading to gradual performance degradation over time.<sup>13</sup> Other materials also such as  $\text{CuO}$  with  $\text{Cu}^{2+14}$  content and  $\text{Mn}_3\text{O}_4$ <sup>15</sup> facing low stability for long term usage. In contrast, tungsten trioxide ( $\text{WO}_3$ ) offers a more structurally stable<sup>16</sup> alternative with defect reversibility due to polaronic behavior where the photoexcited electron localize on tungsten sites with the local structure distortion  $\text{W}^{6+}$  to  $\text{W}^{5+}$ .<sup>17,18</sup> which is similar with  $\text{Fe}^{2+}/\text{Fe}^{3+}$  making it a promising material for sustained hydroxyl radical generation.

Moreover, the utilization of electrons to generate hydroxyl radicals ( $\bullet\text{OH}$ ) allows the holes in  $\text{WO}_3$  to be more freely available for driving chemical reactions which enable  $\text{WO}_3$  as photo-Fenton like reaction as well as photocatalytic reaction. Several studies have reported that the holes in  $\text{WO}_3$  can promote the Oxygen Evolution Reaction (OER) in the presence of electron scavengers such as  $\text{Ag}^+$  and  $\text{Fe}^{3+}$ .<sup>19</sup> However, the activation of OER in these systems is limited due to the non-recyclable nature of the scavenging process. In contrast, in the Photo-Fenton-like reaction using  $\text{WO}_3$ , the electron scavenging process is expected to be efficiently recyclable, which could lead to enhanced OER efficiency.



Therefore, in this study, the novel utilization of both charge carriers in the direct photo-Fenton-like reaction of  $\text{WO}_3$  by acknowledging the polaronic behavior of  $\text{WO}_3$  was investigated. Recently, interesting polaron behavior in small nanoparticles driven by lattice distortion are reported for metal oxides including particle size effects and surface heterogeneity of polaron,<sup>20–23</sup> and thus nanoparticle synthesis of  $\text{WO}_3$  is also expected to exploit polaronic behavior. The utilization of both charge carriers, electrons and holes, by the photo-Fenton reaction was monitored by wastewater removal for electrons and oxygen evolution reaction for holes at the same time. Currently, the usage of photo-Fenton-like reaction of  $\text{WO}_3$  always requires iron support to activate the reactions<sup>24,25</sup> which are probably attributed to the inefficient polaron formation of  $\text{WO}_3$ . Therefore, in this study, the efficiency of the polaron formation was further optimized by understanding the growth of  $\text{WO}_3$ , which is controlled by the control of protonation process, enabling us to understand the crystallization difference that affects the photo-Fenton like efficiency. This study will provide new insights into the utilization of  $\text{WO}_3$  as a catalytic material for promoting chemical reactions.

## 2. EXPERIMENTAL DETAIL

### 2.1 $\text{WO}_3$ synthesis

Initially, 3.3 g of disodium tungstate dihydrate ( $\text{Na}_2\text{WO}_4 \cdot 2\text{H}_2\text{O}$ ) (Fujifilm Wako Pure Chemical co.) was dissolved in 200 mL of deionized water under continuous stirring with a magnetic stirrer. Once fully dissolved, the solution was protonated by adding varying amounts of 37% HCl (Fujifilm Wako Pure Chemical co.). The protonation process was controlled by adjusting the volume of HCl to 15 mL, 30 mL, 60 mL, and 180 mL, corresponding to proton concentration ( $[\text{H}^+]$ ) were 0.8, 1.6, 2.8 and 5.7 M (**Supporting Information, (S1)**), hereafter referred to as  $[\text{H}^+]$



= 0.8,  $[H^+] = 1.6$ ,  $[H^+] = 2.8$ , and  $[H^+] = 5.7$ , respectively. The solution was stirred continuously for 12 hours at room temperature. After stirring, the precipitate was collected by centrifugation and washed with deionized water until the pH of the supernatant reached 4–5. The washed sample was then dried under vacuum at 60 °C for 12 hours. Finally, the dried products underwent annealing at 400 °C for 2 hours under ambient air atmosphere, yielding the final  $WO_3$  product.

## 2.1 Materials characterization

The morphology of the particles was investigated by transmission electron microscope (JEM-2100Plus, JEOL, Japan). Crystal structure and crystallite size were determined using X-ray powder diffraction (XRD, Rigaku SmartLab 9MTP, Japan) with a  $Cu\ K\alpha$  ( $\lambda = 1.5418\ \text{\AA}$ ) radiation sources at 3°/min. The  $2\theta$  scanning range is 20–80°. The chemical states of the samples were investigated by X-ray photoelectron spectroscopy (XPS; PHI5600, ULVAC-PHI, Japan.) which was performed using monochromatized X-rays of  $Al\ K\alpha$  with 300 W power source, the fitting of tungsten elements were conducted from 33 to 40 eV with Shirley baseline methods. The optical absorption of was monitored by UV-Vis-NIR V-770TWK, JASCO, Japan and the luminescence analysis was investigated by Fluorescence Spectrophotometer (FL), F-2700 Hitachi High-Technologies, Japan. The local structure of  $WO_3$  was further characterized by a microscopic confocal Raman spectroscopy (HORIBA LabRAM HR-800, Japan) with an excitation wavelength of 532 nm. The defect analysis then investigated by electron paramagnetic resonance (EPR) (B Bruker BioSpin, Bruker, Germany).

## 2.2. Photo-Fenton like reaction



The photo-Fenton-like reaction was evaluated by monitoring the degradation of Acid Orange 7 in the presence of  $\text{WO}_3$ ,  $\text{H}_2\text{O}_2$ , and UV light (detailed experimental set-up see **Supporting Information, (S2)**). Typically, a  $20 \text{ mg L}^{-1}$  Acid Orange 7 solution was prepared in 50 mL of water. The pH was then adjusted to 2 by adding a 10% HCl solution. Afterwards,  $40 \text{ mg L}^{-1}$  of the  $\text{WO}_3$  catalyst was added, and the suspension was stirred for 30 minutes under a  $200 \text{ mL min}^{-1}$   $\text{N}_2$  atmosphere to ensure sufficient adsorption–desorption equilibrium. Subsequently, 2 mL of 30%  $\text{H}_2\text{O}_2$  was introduced and stirred for 5 minutes. The mixture was then irradiated using a 22 W UV lamp (approx.:  $70 \text{ mW cm}^{-2}$ , 365 nm). A 3 mL aliquot of the solution was collected, centrifuged to remove residual particles, and analyzed by UV–Vis spectroscopy (JASCO V-570, Japan). Meanwhile, 0.5 mL of the evolved gas was sampled and injected into a gas chromatograph (GC–Shimadzu 2014, Japan) equipped with a thermal conductivity detector to identify gaseous products (detailed calibration procedures are provided in the **Supporting Information, (S2)**). For  $\bullet\text{OH}$  detection via the terephthalic acid fluorescence method, 0.04 g of  $\text{WO}_3$  catalyst was dispersed in a  $\sim 4.8 \times 10^{-4} \text{ M}$  terephthalic acid solution, followed by the addition of 2 mL of  $\text{H}_2\text{O}_2$ . The suspension was then irradiated under UV light. After irradiation, fluorescence intensity was measured using a Fluorescence Spectrophotometer (F-2700, Hitachi High-Technologies, Japan) at an excitation wavelength of 325 nm. For the scavenger experiments, two scavengers were employed: 0.059 mmol silver nitrate ( $\text{AgNO}_3$ ) as an electron scavenger and 21 mmol tert-butanol as an  $\bullet\text{OH}$  radical scavenger. Each scavenger was added separately to the photo-Fenton-like reaction system, and the corresponding degradation performance was subsequently monitored.

### 3. RESULTS AND DISCUSSION

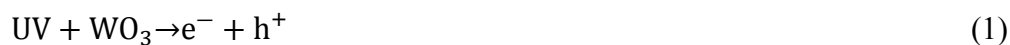
**Figure 1(a)** illustrates the degradation of Acid Orange 7 under different reaction conditions. Under  $\text{WO}_3$  with UV light and  $\text{WO}_3$  with  $\text{H}_2\text{O}_2$  there are no degradations observed, indicating that neither



process alone facilitates a redox reaction. However, when  $\text{H}_2\text{O}_2$  is exposed to UV light ( $\text{H}_2\text{O}_2 + \text{UV}$ ), approximately 10% degradation occurs, likely due to the generation of hydroxyl radicals from  $\text{H}_2\text{O}_2$  under UV irradiation.<sup>26</sup> In contrast, a significant increase in degradation efficiency is observed when combining UV light,  $\text{WO}_3$ , and  $\text{H}_2\text{O}_2$ , reaching approximately 50% degradation. This strong degradation suggests a synergistic effect among UV light,  $\text{WO}_3$ , and  $\text{H}_2\text{O}_2$ .

The high degradation efficiency observed only in the presence of  $\text{WO}_3$ , UV light, and  $\text{H}_2\text{O}_2$  has similarity with the Photo-Fenton reaction, where  $\text{Fe}^{2+}$  reacts with  $\text{H}_2\text{O}_2$  and UV light to accelerate hydroxyl radical generation.<sup>26,27</sup> Given this similarity, it is highly likely that a similar mechanism occurs in  $\text{WO}_3$ . To clarify this assumption, XPS analysis of the W 4f state before and after UV irradiation was performed, as shown in **Figures 1(b)–(c)**. The results reveal a gradual increase in the  $\text{W}^{5+}$  content from 2.5% to 3.6% after UV irradiation. This transition is also visually confirmed by the photographic evidence in **Figure 1(d)**, which shows a distinct color change from bright yellow to a greenish hue, attributed to the formation of  $\text{W}^{5+}$ , a phenomenon known as photochromism.<sup>28,29</sup>

The transition from  $\text{W}^{6+}$  to  $\text{W}^{5+}$  plays a crucial role in promoting the Photo-Fenton-like reaction, as described by the following reaction pathway:





Under UV irradiation,  $\text{WO}_3$  generates electron-hole pairs, where photogenerated electrons reduce  $\text{W}^{6+}$  to  $\text{W}^{5+}$  on the surface while holes on O 2p states trapped in oxygen sites ready for promoting possible chemical reaction.<sup>30</sup> The  $\text{W}^{5+}$  species then interact with  $\text{H}_2\text{O}_2$ , further promoting the formation of hydroxyl radicals which decompose Acid Orange 7 into carbon dioxide (Direct evidence of  $\text{CO}_2$  evolution has been shown in the **Supporting Information, (S3)** and water, as illustrated in **Figure 1(e)**). Interestingly, the Photo-Fenton-like activity of  $\text{WO}_3$  shows better catalytic reaction than traditional Fenton reaction either by using  $\text{FeCl}_2$  ion and  $\text{Fe}_2\text{O}_3$  nanoparticles as shown in **Table 1** which highlight the strong potential of  $\text{WO}_3$  as an effective material for waste-water degradation by photo-Fenton reactions.

While the electron continuously generates  $\cdot\text{OH}$  through photo-Fenton like reaction process, holes in the valence band are ready to promote chemical reactions. There are two possible reactions for holes in these reaction conditions. The first one is the reaction with  $\text{OH}^-$  for generating  $\cdot\text{OH}$ . This reaction is one of the common reactions for  $\text{WO}_3$ , where  $\text{WO}_3$  has been acknowledged as good oxidative photocatalyst.<sup>31</sup> However, based on the catalytic reaction process, if  $\cdot\text{OH}$  is formed, the degradation of Acid Orange 7 should occur even without  $\text{H}_2\text{O}_2$ . It indicates that the  $\cdot\text{OH}$  radicals are not formed in this reaction condition. The second possibility is the water oxidation process where holes directly oxidize water into  $\text{O}_2$  and  $\text{H}^+$ .<sup>19</sup>

To confirm the second reaction possibility, oxygen evolution during the Photo-Fenton-like reaction was investigated. To eliminate the possibility of  $\text{O}_2$  release from direct  $\text{H}_2\text{O}_2$  decomposition, a control experiment was conducted using  $\text{H}_2\text{O}_2$  under UV irradiation alone. The calibration details for the  $\text{O}_2$  evolution reaction are provided in **Supporting Information, (S2)**. As shown in **Figure 1(f)**, UV irradiation of  $\text{H}_2\text{O}_2$  alone generates approximately  $0.62 \text{ mmol g}^{-1}$  of  $\text{O}_2$ ,



with an  $O_2$  evolution rate of about  $0.21 \text{ mmol}\cdot\text{g}^{-1}\cdot\text{h}^{-1}$ . In the presence of  $WO_3$  under UV irradiation, the  $O_2$  production increases significantly to  $3.1 \text{ mmol}\cdot\text{g}^{-1}$ , confirming the enhanced photocatalytic activity. To exclude the contribution from  $H_2O_2$  photodecomposition, the  $O_2$  evolution rates were corrected by subtracting  $0.21 \text{ mmol}\cdot\text{g}^{-1}\cdot\text{h}^{-1}$ . After correction, the  $O_2$  evolution rate for  $WO_3$  under UV irradiation is approximately  $0.80 \text{ mmol}\cdot\text{g}^{-1}\cdot\text{h}^{-1}$  and further increases to about  $1.62 \text{ mmol}\cdot\text{g}^{-1}\cdot\text{h}^{-1}$  when  $WO_3$  is combined with  $H_2O_2$  (see **Supporting Information, (S4)**). These results demonstrate that both photogenerated electrons and holes in  $WO_3$  are effectively utilized, overcoming the previously reported limitations associated with  $WO_3$  photocatalysis. Furthermore, the  $O_2$  evolution performance achieved in this work is higher than values reported in the literature (**Table 1**), reinforcing the enhanced photo-Fenton-like activity of  $WO_3$ .

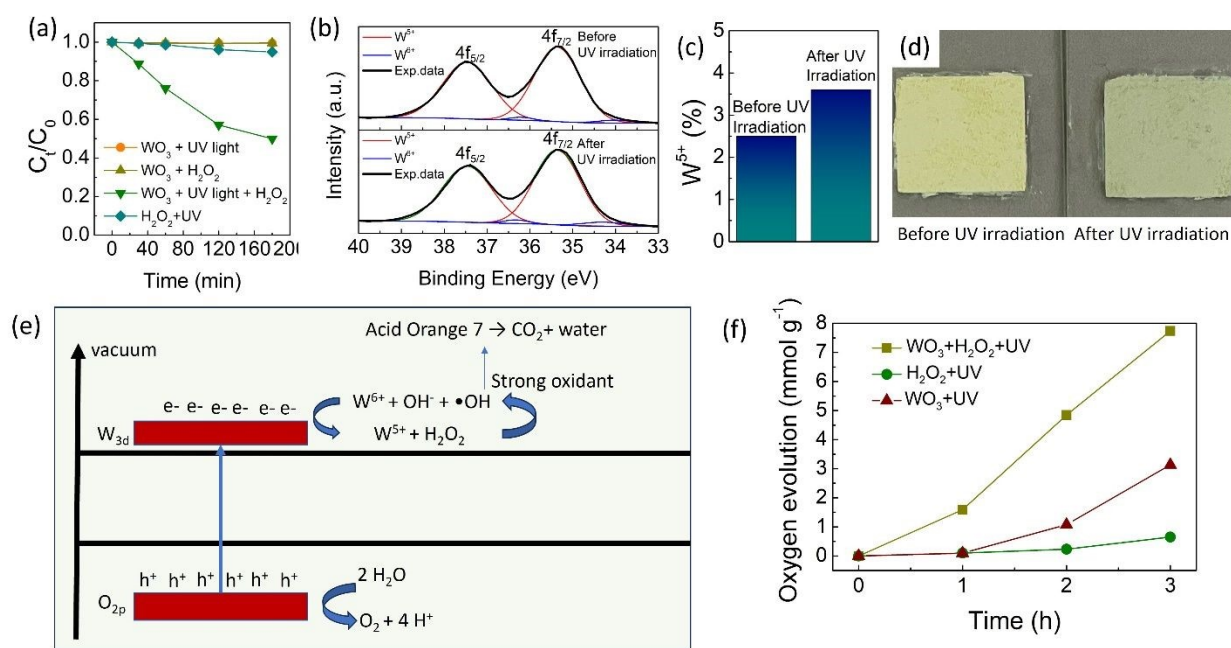


**Figure 1.** (a) Acid Orange 7 degradation under various systems. (b) XPS analysis of  $WO_3$  before and after UV irradiation. (c)  $W^{5+}$  percentage obtained from XPS deconvolution. (d) Photographic images of  $WO_3$  before and after reaction. (e) Proposed photo-Fenton reaction by using  $WO_3$ . (f) Oxygen evolution reaction by  $WO_3 + H_2O_2 + \text{UV}$  compared with  $WO_3 + \text{UV}$  and  $H_2O_2 + \text{UV}$ .



**Table 1.** Photocatalytic performance for Acid Orange 7 degradation and oxygen evolution reaction of Polaron  $\text{WO}_3 + \text{H}_2\text{O}_2$  compared with other reports and data.

Sample	degradation rates ( $\text{h}^{-1}$ )	References	Sample	$\text{O}_2$ Evolution rate ( $\text{mmol g}^{-1}$ $\text{h}^{-1}$ )	References
$\text{Fe}_2\text{O}_3 + \text{H}_2\text{O}_2$	0.06	32	$\text{Fe} + \text{TiO}_2$	0.54	33
$\text{Fe}_2\text{O}_3 + \text{H}_2\text{O}_2$	0.13	34	$\text{Ag} + \text{TiO}_2$	0.06	35
$\text{Fe} + \text{H}_2\text{O}_2$	0.03	This works	$\text{FeOOH} + \text{WO}_3 + \text{H}_2\text{O}_2$	0.03	25
Polaron $\text{WO}_3 + \text{H}_2\text{O}_2$	0.18	This works	Polaron $\text{WO}_3 + \text{H}_2\text{O}_2$	1.62	This works

The  $\text{WO}_3$ -based photo-Fenton-like reaction has been demonstrated; however, the degradation efficiency remains relatively low (50% in 180 minutes). Therefore, further optimization strategies are necessary. The key to enhancing the photo-Fenton-like activity in  $\text{WO}_3$  lies in the generation of  $\text{W}^{5+}$  species. Increasing the formation of  $\text{W}^{5+}$  under UV irradiation is essential. Previous studies have proposed that defect engineering can play a crucial role in promoting  $\text{W}^{5+}$  generation,<sup>36</sup> such as hydrogen annealing<sup>37</sup> or doping<sup>38,39</sup>, can improve photochromism. However, these approaches introduce additional processing steps and materials, reducing overall efficiency.

Different from the above-mentioned techniques, the control of the nucleation and growth process during synthesis also provides a controllable of lattice behavior including strain and defect, which is insightful for improving  $\text{W}^{5+}$  formation in  $\text{WO}_3$ . In this study,  $\text{W}^{5+}$  formation was improved by regulating crystal growth through modulating the protonation level during synthesis. The proton concentration varied from  $[\text{H}^+] = 0.8, 1.6, 2.8$  and  $5.7$ . Initially the precursors are still in the form of  $(\text{H}_4\text{WO}_5)$  (see XRD and TEM results in **Supporting Information, (S5)**) and reduces



the particle size of the precursor as increase of the protonation indicating the increase of the supersaturation process due to high protonation. After annealing treatment, the stable  $\text{WO}_3$  is formed (detail structure analysis at **Figure 4(a)-(b)**). The change in the acid concentration significantly affects  $\text{W}^{5+}$  formation in the  $\text{WO}_3$  structure. **Figure 2(a)** shows images of  $\text{WO}_3$  at different protonation levels after UV irradiation. Clear evidence demonstrates that after UV irradiation, the color gradually changed to dark green as protonation increased, indicating an enhancement in  $\text{W}^{5+}$  generation. XPS analysis of W4f after and before UV irradiation has confirmed that the  $\text{W}^{5+}$  gradually increase with increasing protonation level from  $[\text{H}^+]$  0.8 to 5.7 (**Figure 2(b)**). **Table 2** also shows the detail of  $\text{W}^{5+}$  percentages after UV irradiation which indicates a gradually increase with increase of protonation. Besides  $\text{W}^{5+}$  formation, the  $\text{N}_2$  adsorption desorption analysis results (**Figure 2(c)**) have revealed that the high protonation also increases the surface area, pore size and pore volumes of  $\text{WO}_3$  as tabulated in **Table 2**.

**Table 2.**  $\text{W}^{5+}$  concentration, and physical surface properties of  $\text{WO}_3$  at different protonation.

Sample	$\text{W}^{5+}$ % after irradiation	Surface Area ( $\text{m}^2 \text{g}^{-1}$ )	Pore Size (nm)	Pore Volume ( $\text{cc g}^{-1}$ )
$[\text{H}^+] = 0.8$	2.2	15	3.061	0.066
$[\text{H}^+] = 1.6$	3.6	24	2.178	0.244
$[\text{H}^+] = 2.8$	5.5	29	29.47	0.331
$[\text{H}^+] = 5.7$	6.7	37	32.50	0.247

The influence of increasing protonation was further evaluated through the photo-Fenton reaction. **Figure 2(d)–(e)** presents the Acid Orange 7 degradation profiles at different protonation levels. The degradation efficiency of  $\text{WO}_3$  increases progressively with higher protonation, with



the reaction rate rising from 0.18 to 0.68 h<sup>-1</sup>. This trend clearly indicates that protonation enhances the photo-Fenton activity. At this stage, two major factors appear to affect the photo-Fenton performance: (i) the formation of W<sup>5+</sup> species and (ii) the changes in surface properties. To clarify their respective contributions, several additional analyses were performed. First, the adsorption of Acid Orange 7 on WO<sub>3</sub> was examined to evaluate the influence of surface characteristics. As shown in the **Supporting Information, (S6)**, Acid Orange 7 adsorption increases slightly with increasing surface area, with approximately 5% removal observed. This indicates that surface properties also contribute to the degradation process. This conclusion is further supported by the surface charge analysis and photo-Fenton-like reactions performed at different pH values (**Supporting Information, (S7)**) where the surface charge and types of pollutant affected the photo-Fenton reactions, both of which confirm that surface characteristics play a role in accelerating the photo-Fenton reaction. On the other hands, to assess the contribution of W<sup>5+</sup> species, photo-Fenton reactions were conducted using samples with comparable surface areas but different internal defect (W<sup>5+</sup>) concentrations conducting by heated the [H<sup>+</sup>] = 5.7 precursor under air and nitrogen atmosphere (see **Supporting Information, (S8)**). The results clearly show that the higher W<sup>5+</sup> significantly enhances the degradation rate although the surface area nearly similar. Taken together, these data demonstrate that the improved photo-Fenton performance arises from the synergistic effect between increased formation of W<sup>5+</sup> and the enhancement of surface properties induced by protonation. While surface properties mainly influence the attachment of Acid Orange 7 onto WO<sub>3</sub>, the formation of W<sup>5+</sup> is primarily responsible for promoting the conversion of H<sub>2</sub>O<sub>2</sub> into •OH radicals.

**Figure 2(f)** presents the terephthalic acid fluorescence analysis, confirming •OH generation under irradiation. The samples with higher protonation exhibit the highest fluorescence



intensity, indicating enhanced  $\bullet\text{OH}$  production which correlated with improvement of Acid Orange 7 degradation. However, although  $\bullet\text{OH}$  plays a key role in Acid Orange 7 degradation, the initial process was starting from the photoexcitation of electrons that generate  $\text{W}^{5+}$ , which then reacts with  $\text{H}_2\text{O}_2$  to produce  $\bullet\text{OH}$  radicals. This conclusion is further supported by the scavenger experiments shown in **Figure 2(g)**, where the presence of electron scavengers results in the greatest suppression of catalytic activity, clearly demonstrating that electron-driven polaron formation is the major contributor to the overall reaction.

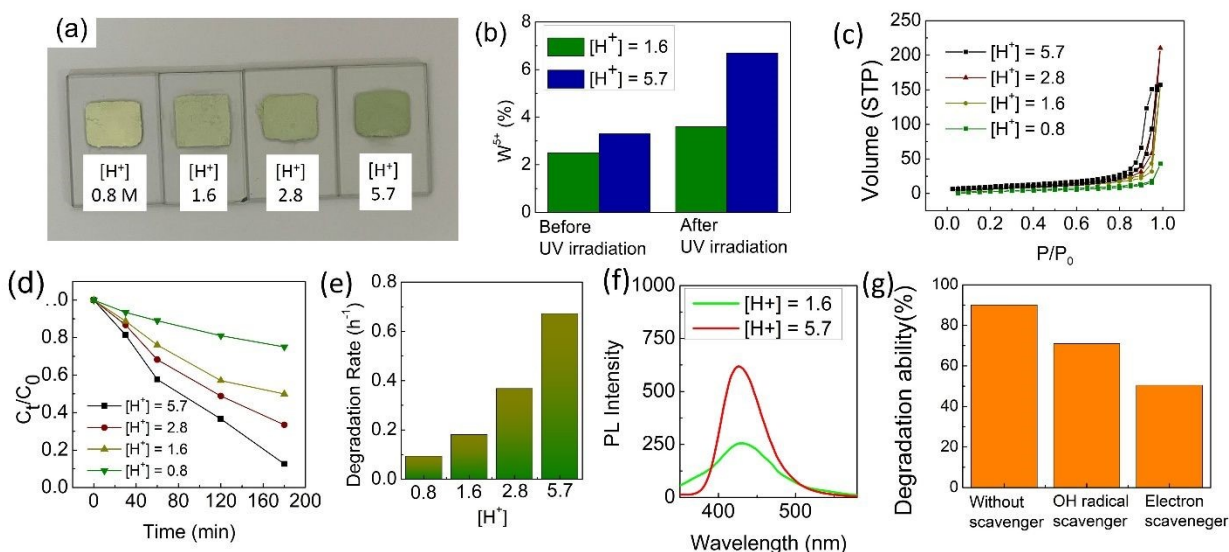


**Figure 2.** (a) Photographic images of  $\text{WO}_3$  samples with different protonation levels after UV irradiation. (b)  $\text{W}^{5+}$  percentages before and after UV irradiation, obtained from XPS analysis of the W 4f region. (c)  $\text{N}_2$  adsorption–desorption isotherms of  $\text{WO}_3$  samples with different protonation levels. (d) Acid Orange 7 degradation profiles for  $\text{WO}_3$  samples with varying protonation. (e) Degradation rate constants for Acid Orange 7 using  $\text{WO}_3$  with different protonation levels. (f) Fluorescence analysis using terephthalic acid to detect  $\bullet\text{OH}$  radical generation for  $[\text{H}^+] = 1.6$  and  $5.7$ , and (g) scavenger tests using  $\bullet\text{OH}$  scavengers and electron scavengers.

To assess the potential of this photo-Fenton-like reaction by applications, the degradation of other types of pollutants was also investigated (**Figure 3(a)**). Cationic dyes, represented by methylene blue, and pharmaceutical waste, represented by 4-Nitrophenol, were studied. The



results show that the photo-Fenton reaction using  $\text{WO}_3$  with high  $\text{W}^{5+}$  effective in degrading various types of pollutants, demonstrating its potential for future wastewater management applications.

The improvement of electron site efficiency is directly correlated with the improvement in the hole efficiency. As shown in **Figures 3(b)**, the OER rate increases steadily from  $1.62 \text{ mmol g}^{-1} \text{ h}^{-1}$  to  $3.66 \text{ mmol g}^{-1} \text{ h}^{-1}$ . This data demonstrates a clear correlation between the enhanced photo-Fenton-like reaction, driven by increase in  $\text{W}^{5+}$  attributed to the increase of protonation. However, as shown in the mechanism section **Figure 1(e)**, the recycling process should occur during reaction which means that the  $\text{WO}_3$  should have good recyclability to be used several times. For clarifying these phenomena, the repeatability test was also conducted to assess the recyclability of the photo-Fenton reaction. The data plotted in **Figure 3(c)** shows the good stability of oxygen evolution reaction and dye degradation after 4 recycle experiments which further elevated the potential of this concept for practical applications. This stability test confirmed the advantages of photo-Fenton like reaction by using  $\text{WO}_3$  which shows better catalytic stability compared to traditional iron ion,  $\text{TiO}_2$ ,<sup>13</sup>  $\text{CuO}$ ,<sup>14</sup> and  $\text{Mn}_3\text{O}_4$ .<sup>15</sup>

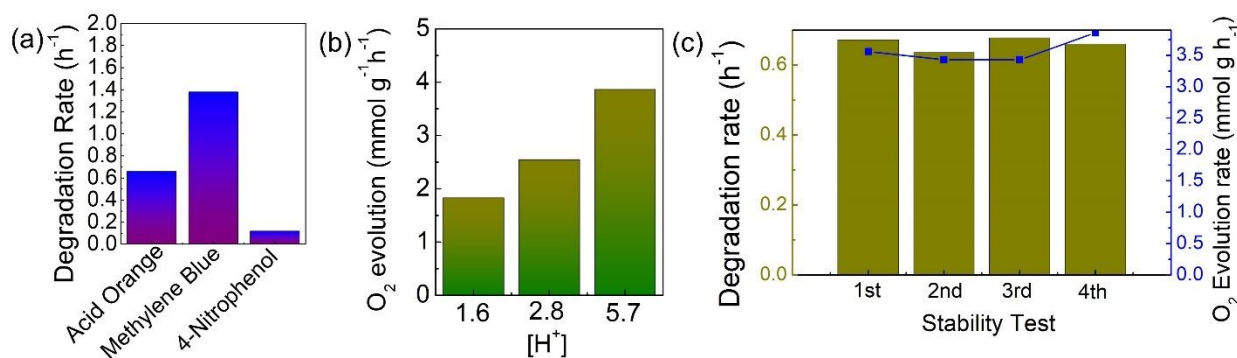


**Figure 3.** (a) Degradation ability of  $[\text{H}^+] = 5.7$  sample for degrading other types of wastewaters. (b) Oxygen evolution rate for different protonation samples. (c) Stability of the  $[\text{H}^+] = 5.7$  catalysts in terms of the reaction rate for Acid Orange 7 removal and oxygen evolution reaction.



The enhancement of the photo-Fenton-like reaction has been clarified with relatively satisfactory results through increasing protonation. However, the origin of the increase in surface area and  $W^{5+}$  formation during UV irradiation, along with the gradual increase in protonation, needs to be clarified in detail. One major question is clarifying the crystal growth behavior under different protonation levels, which affects the ease of  $W^{5+}$  formation and surface properties. Initially, XRD patterns were analyzed to investigate the crystal structure of  $WO_3$  at different protonation levels. As shown in **Figure 4(a)**, the diffraction patterns exhibit the characteristic peaks corresponding to monoclinic  $WO_3$  (JCPDS No. 83-0950) with a space group of  $P21/n$ . Rietveld refinement performed using the Profex (open-source) software confirms that all patterns can be well-fitted with a single  $WO_3$  phase, indicating the absence of any secondary phases. No diffraction peaks associated with  $H_4WO_5$  were detected in any of the samples. **Supporting information (S9)** further shows that at 400 °C,  $H_4WO_5$  is fully transformed into the  $WO_3$  structure.





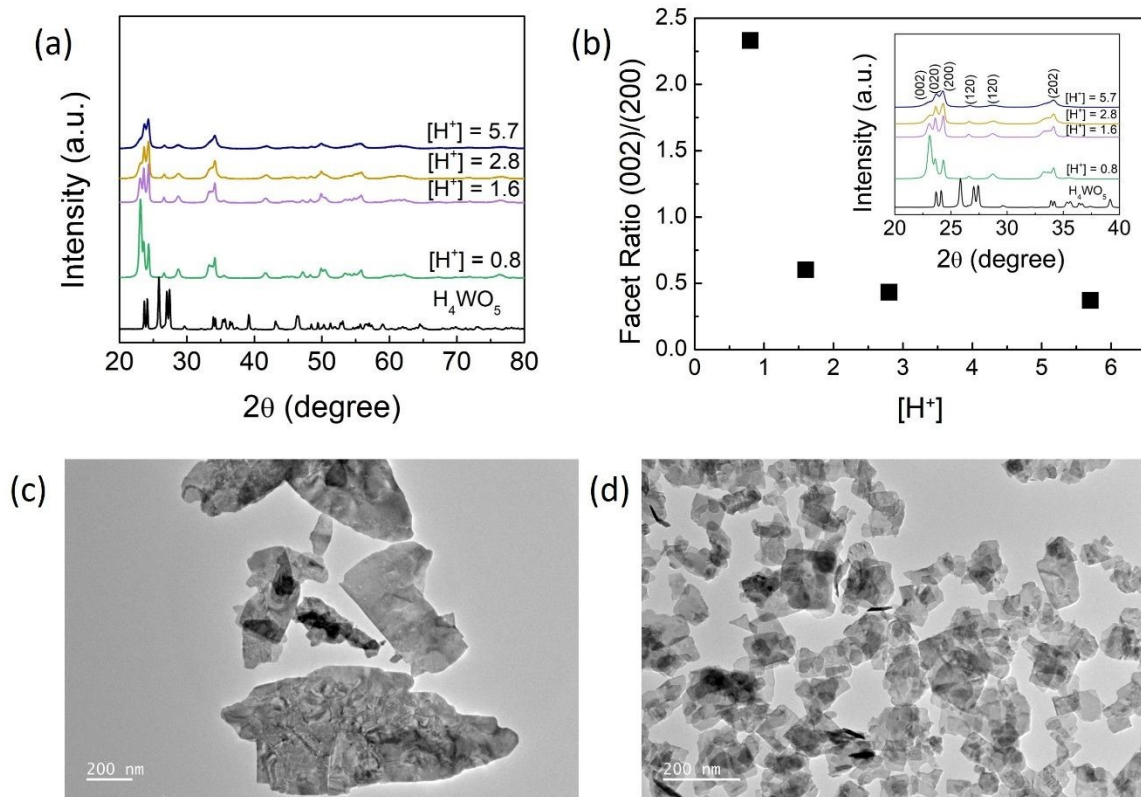


**Figure 4.** (a) XRD spectra of  $\text{WO}_3$  prepared at different protonation. (b) Intensity ratio between (002) facet with (200) facet (inset shows XRD spectra of  $\text{WO}_3$  prepared at different protonation with narrow angle ranges). TEM images of  $\text{WO}_3$  for (c)  $[\text{H}^+] = 0.8$  and (d)  $[\text{H}^+] = 5.7$  samples.

Although all samples crystallize in the monoclinic  $\text{WO}_3$  phase, the intensity of the (002) reflection decreases progressively with increasing protonation (inset of **Figure 4(b)**). The intensity ratio of the (002) to (200) planes decrease sharply from 2.33 for  $[\text{H}^+] = 0.8$  to 0.33 for  $[\text{H}^+] = 5.7$ , indicating a significant change in the relative growth orientation associated with protonation. The (002) peak is usually correlated with the lateral dimension of the material. With the gradual decrease in the (002) peak, there is a possibility that the lateral dimension also decreases, indicating a reduction in particle size as confirmed by TEM analysis (**Figure 4(c)** and **(d)**) attributed to the increase in supersaturation degree which increase the number of nuclei formations and decrease the particle growth. It is easy to understand that this smaller size correlated with surface area



enhancement. On the other hand, to find the origin of high  $W^{5+}$  formation during UV irradiation, additional analysis is required.

The detail crystal structure analysis at different protonation levels then analyzed by examining the changes in lattice volume and lattice parameters, as shown in **Figure 5(a)**. An expansion in lattice volume was observed with increasing supersaturation process attributed to the different protonation levels during synthesis. The lattice strain then estimated by comparing the lattice structure of high crystalline  $WO_3$  with the current samples (see **Supporting Information, (S10)**). The results show that the higher protonation, the increase in the tensile strain from 0.21 % to 0.79 %. The expansion of the lattice might be correlated with the distortion of the lattice crystals by protonation. For confirming the distortion in the crystal, Raman spectroscopy was performed to analyze the chemical bonding between tungsten and oxygen atoms (**Figure 5(b)**). Two distinct peaks were observed in the range of 500–1000  $cm^{-1}$  at 806  $cm^{-1}$  and 712  $cm^{-1}$ , corresponding to the stretching vibrations of W–O–W bonds<sup>41,42</sup>. Notably, peak broadening at 712  $cm^{-1}$  became more pronounced with increasing protonation, indicating increased lattice distortion. Additionally, a shoulder peak at 637  $cm^{-1}$  emerged and intensified with higher protonation levels. This feature, absent in highly crystalline  $WO_3$ , further confirms the progressive distortion of the crystal structure with increasing protonation.



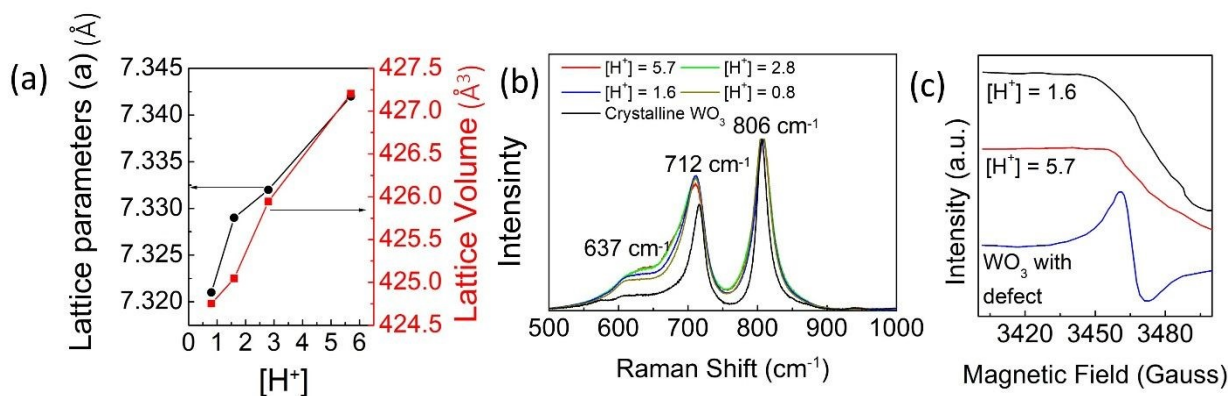


**Figure 5.** (a) Lattice parameters analysis of  $\text{WO}_3$  with different protonation levels. (b) Raman spectra of  $\text{WO}_3$  prepared at different protonation levels. (c) EPR analysis of  $\text{WO}_3$  for  $[\text{H}^+] = 1.6$ ,  $[\text{H}^+] = 5.7$ , and defect vacancy existed  $\text{WO}_3$ .

The origin of lattice distortion can be attributed to several factors, including strain and oxygen vacancy defects. To determine the primary cause, electron paramagnetic resonance (EPR) analysis was performed on  $\text{WO}_3$  samples with different protonation levels to confirm the formation of lattice defects (vacancies) (**Figure 5(c)**). Additionally, defective  $\text{WO}_3$  was provided as a comparison to confirm the presence of oxygen vacancies by annealing the  $[\text{H}^+] = 5.7$  under  $\text{N}_2$  atmosphere for 400 °C for 2h. A distinct signal was observed at 3450–3480 gauss, characteristic of oxygen vacancy formation. However, no corresponding oxygen vacancy signals were detected for  $\text{WO}_3$  samples with  $[\text{H}^+] = 1.6$  and  $[\text{H}^+] = 5.7$ . Instead, distortion is likely induced by strain attributed to the rapid supersaturation process where at high supersaturation rapid nucleation occurs, which limits crystal growth and introduces structural disorder.

The strain-modulated enhancement of  $\text{W}^{5+}$  formation and its influence on the reaction process has been confirmed. However, the precise origin of the strain effect on  $\text{W}^{5+}$  formation remains unclear. Several researchers have suggested that strain can induce electron localization,



allowing electrons to remain longer on the surface.<sup>23,43,44</sup> This phenomenon was further validated in the case of WO<sub>3</sub>. As shown in the photoluminescence analysis (**Supporting information, (S11)**), the peak intensity at [H<sup>+</sup>] = 5.7 is lower than that at [H<sup>+</sup>] = 1.6, indicating that electrons spend more time in the conduction band, thereby promoting polaron formation. Enhanced electron localization due to strain was also confirmed by spin-polarized density functional theory calculations, which revealed an increase in total magnetization from 2.83 μB in the unstrained structure to 3.14 μB in the strained structure (**Supporting Information, (S12)**). Collectively, these results demonstrate that strained WO<sub>3</sub> more readily localizes electrons and promotes polaronic behavior, thereby accelerating the photo-Fenton reaction.

## CONCLUSION

In this study, a novel concept has been successfully introduced for the utilization of charge carriers in WO<sub>3</sub> through a photo-Fenton-like reaction. Light induced on WO<sub>3</sub> promotes the excitation of electrons, reducing W<sup>6+</sup> to W<sup>5+</sup>, which interacts with H<sub>2</sub>O<sub>2</sub> to produce •OH that was successfully utilized for wastewater remediation. On the other hand, the holes in the valence band efficiently conduct water splitting to produce O<sub>2</sub>, attributed to the trapping of electrons that promotes the photo-Fenton-like reaction. The photo-Fenton-like reaction was optimized by controlling protonation during synthesis, which regulates crystal growth. Higher protonation resulted in smaller particle sizes, larger surface areas, and increased W<sup>5+</sup> content, attributed to the higher crystal strain. These changes in physical and electronic properties enhance the ability of WO<sub>3</sub> to drive the photo-Fenton-like reaction for Acid Orange 7 degradation and the oxygen evolution reaction, owing to the synergistic effect between surface chemistry and W<sup>5+</sup> formation. Overall, these findings demonstrate the efficient charge utilization of WO<sub>3</sub> in photo-Fenton-like processes.



## AUTHOR INFORMATION

### Corresponding Author

\*Corresponding author. E-mail: ardiansyah.taufik.d2@tohoku.ac.jp;

tadafumi.ajiri.b1@tohoku.ac.jp; akira.yoko.c7@tohoku.ac.jp;

### Conflicts of interest

There are no conflicts to declare.

### Data availability

The data supporting this article have been included as part of the Supplementary Information.

### Author Contributions

The manuscript was written through contributions of all authors. All authors have given approval to the final version of the manuscript.

## ACKNOWLEDGMENT

The authors acknowledge the support from the Japan Science and Technology Agency (JST) [MIRAI, Grant Number JPMJMI17E4 and CREST, Grant Number JPMJCR16P3], the New Energy and Industrial Technology Development Organization of Japan (NEDO), JSPS KAKENHI (Grant Numbers JP16H06367, JP20K20548, and JP21H05010), Materials Processing Science Project (Materealize; Grant Number JPMXP0219192801) of the Ministry of Education, Culture, Sports, Science and Technology (MEXT), Professional Development Consortium for



Computational Materials Scientists (PCoMS), and the World Premier International Research Center Initiative (WPI), MEXT, Japan. The Analytical Research Core for Advanced Materials, Institute for Materials Research, Tohoku University for JEM-ARM-200F measurement.

## REFERENCES.

1. Chen, Q.; Lü, F.; Qiu, J.; Zhang, H.; He, P. Pathways and Selectivity of Fenton Degradation of Different Precursor Species of Dissolved Organic Matter. *Nature Communications* 2025, *16* (1). <https://doi.org/10.1038/s41467-025-61753-7>.
2. Huang, M.; Liu, H. Z.; Huang, Q. Q.; Zhou, T.; Wu, X.; Li, W. W.; Yu, H. Q. Self-Activated Heterogeneous Fenton Process for Accelerated Degradation of Aromatic Pollutants over Copper Oxide Catalysts. *Angewandte Chemie - International Edition* 2025, *64* (30). <https://doi.org/10.1002/anie.202508754>.
3. Yan, Q.; Lian, C.; Huang, K.; Liang, L.; Yu, H.; Yin, P.; Zhang, J.; Xing, M. Constructing an Acidic Microenvironment by MoS<sub>2</sub> in Heterogeneous Fenton Reaction for Pollutant Control. *Angewandte Chemie - International Edition* 2021, *60* (31), 17155–17163. <https://doi.org/10.1002/anie.202105736>.
4. Manikandan, V.; Elango, D.; Subash, V.; Kumar, P.; Packialakshmi, J. S.; Jayanthi, P.; Sun, Y. J.; Song, K. S. Needle ZrO<sub>x</sub> Loaded NiFe<sub>2</sub>O<sub>4</sub> Catalysts for Photo-Fenton Degradation of Bisphenol A and 4 Nitrophenol. *NPJ Clean Water* 2025, *8* (1). <https://doi.org/10.1038/s41545-025-00483-1>.
5. Walling, S. A.; Um, W.; Corkhill, C. L.; Hyatt, N. C. Fenton and Fenton-like Wet Oxidation for Degradation and Destruction of Organic Radioactive Wastes. *npj Materials Degradation*. Nature Publishing Group December 1, 2021. <https://doi.org/10.1038/s41529-021-00192-3>.
6. Zareh, M. M.; El-Sayed, A. S.; El-Hady, D. M. Biosorption Removal of Iron from Water by *Aspergillus Niger*. *NPJ Clean Water* 2022, *5* (1). <https://doi.org/10.1038/s41545-022-00201-1>.
7. Liu, T.; Hu, K.; Li, Y.; Wang, Y.; Han, D.; Wang, Z.; Gu, F. The Z-Scheme MIL-88B(Fe)/BiOBr Heterojunction Promotes Fe(III)/Fe(II) Cycling and Photocatalytic-Fenton-Like Synergistically Enhances the Degradation of Ciprofloxacin. *Small* 2024, *20* (27). <https://doi.org/10.1002/sml.202309541>.
8. Song, Y.; Rong, C.; Shang, J.; Wang, Y.; Zhang, Y.; Yu, K. Synthesis of an Inorganic-Framework Molecularly Imprinted Fe-Doped TiO<sub>2</sub> Composite and Its Selective Photo-Fenton-like Degradation of Acid Orange II. *Journal of Chemical Technology and Biotechnology* 2017, *92* (8), 2038–2049. <https://doi.org/10.1002/jctb.5199>.



9. Wu, Z.; Xiong, Z.; Huang, B.; Yao, G.; Zhan, S.; Lai, B. Long-Range Interactions Driving Neighboring Fe–N<sub>4</sub> Sites in Fenton-like Reactions for Sustainable Water Decontamination. *Nature Communications* 2024, 15 (1). <https://doi.org/10.1038/s41467-024-52074-2>.
10. Yan, J.; Qian, L.; Gao, W.; Chen, Y.; Ouyang, D.; Chen, M. Enhanced Fenton-like Degradation of Trichloroethylene by Hydrogen Peroxide Activated with Nanoscale Zero Valent Iron Loaded on Biochar. *Sci Rep* 2017, 7. <https://doi.org/10.1038/srep43051>.
11. Zhu, Y.; Qiu, S.; Tang, W.; Deng, F.; Ma, F.; Zheng, Y.; Xie, H. Sustainable Fe<sup>3+</sup> Reduction by Fe<sub>3</sub>O<sub>4</sub>@tourmaline in Fenton-like System. *Chemical Engineering Journal* 2022, 437. <https://doi.org/10.1016/j.cej.2022.135480>.
12. Huang, X.; Zhou, H.; Yue, X.; Ran, S.; Zhu, J. Novel Magnetic Fe<sub>3</sub>O<sub>4</sub>/α-FeOOH Nanocomposites and Their Enhanced Mechanism for Tetracycline Hydrochloride Removal in the Visible Photo-Fenton Process. *ACS Omega* 2021, 6 (13), 9095–9103. <https://doi.org/10.1021/acsomega.1c00204>.
13. Qiu, J. yuan; Chen, J. hua; Xiao, B. yuan; Li, X. xing; Wan, T.; Qin, F. hong; Mi, Y.; Huang, Z. yin. Oxygen Deficient TiO<sub>2</sub>-x with Dual Reaction Sites for Activation of H<sub>2</sub>O<sub>2</sub> to Degrade Organic Pollutants. *Catal Letters* 2020, 150 (1), 222–233. <https://doi.org/10.1007/s10562-019-02920-6>.
14. Fang, M.; Zheng, R.; Wu, Y.; Yue, D.; Qian, X.; Zhao, Y.; Bian, Z. CuO Nanosheet as a Recyclable Fenton-like Catalyst Prepared from Simulated Cu(II) Waste Effluents by Alkaline H<sub>2</sub>O<sub>2</sub> Reaction. *Environ Sci Nano* 2019, 6 (1), 105–114. <https://doi.org/10.1039/c8en00930a>.
15. Weng, Z.; Li, J.; Weng, Y.; Feng, M.; Zhuang, Z.; Yu, Y. Surfactant-Free Porous Nano-Mn<sub>3</sub>O<sub>4</sub> as a Recyclable Fenton-like Reagent That Can Rapidly Scavenge Phenolics without H<sub>2</sub>O<sub>2</sub>. *J Mater Chem A Mater* 2017, 5 (30), 15650–15660. <https://doi.org/10.1039/c7ta04042c>.
16. Ortiz, J.; Acosta, D.; Magaña, C. Long-Term Cycling and Stability of Crystalline WO<sub>3</sub> Electrochromic Thin Films Prepared by Spray Pyrolysis. *Journal of Solid State Electrochemistry* 2022, 26 (8), 1667–1676. <https://doi.org/10.1007/s10008-022-05211-0>.
17. Tao, J.; Liu, T. Electron and Hole Polaron Formation and Transport in Monoclinic WO<sub>3</sub> Studied by Hybrid Functional Approach. *Journal of Physical Chemistry C* 2023, 127 (32), 16204–16210. <https://doi.org/10.1021/acs.jpcc.3c03991>.
18. Hassani, H.; Bousquet, E.; He, X.; Partoens, B.; Ghosez, P. The Anti-Distortive Polaron as an Alternative Mechanism for Lattice-Mediated Charge Trapping. *Nature Communications* 2025, 16 (1). <https://doi.org/10.1038/s41467-025-56791-0>.
19. Suzuki, H.; Tomita, O.; Higashi, M.; Abe, R. Tungstic Acids H<sub>2</sub>WO<sub>4</sub> and H<sub>4</sub>WO<sub>5</sub> as Stable Photocatalysts for Water Oxidation under Visible Light. *J Mater Chem A Mater* 2017, 5 (21), 10280–10288. <https://doi.org/10.1039/c7ta01228d>.
20. Zhang, X.; Yoko, A.; Zhou, Y.; Jee, W.; Mayoral, A.; Liu, T.; Guan, J.; Lu, Y.; Keal, T. W.; Buckeridge, J.; Ninomiya, K.; Nishibori, M.; Yamamoto, S.; Matsuda, I.; Adschiri, T.; Terasaki, O.; Woodley, S. M.; Catlow, C. R. A.; Sokol, A. A. Surface-Driven Electron



- Localization and Defect Heterogeneity in Ceria. *J Am Chem Soc* 2025. <https://doi.org/10.1021/jacs.5c10679>.
21. Hao, X.; Yoko, A.; Chen, C.; Inoue, K.; Saito, M.; Seong, G.; Takami, S.; Adschiri, T.; Ikuhara, Y. Atomic-Scale Valence State Distribution inside Ultrafine CeO<sub>2</sub> Nanocubes and Its Size Dependence. *Small* 2018, *14* (42). <https://doi.org/10.1002/sml.201802915>.
  22. Hao, X.; Yoko, A.; Inoue, K.; Xu, Y.; Saito, M.; Chen, C.; Seong, G.; Tomai, T.; Takami, S.; Shluger, A. L.; Xu, B.; Adschiri, T.; Ikuhara, Y. Atomistic Origin of High-Concentration Ce<sup>3+</sup> in {100}-Faceted Cr-Substituted CeO<sub>2</sub> Nanocrystals. *Acta Mater* 2021, *203*. <https://doi.org/10.1016/j.actamat.2020.11.015>.
  23. Yoko, A.; Omura, Y.; Ninomiya, K.; Nishibori, M.; Fujita, T.; Kasai, H.; Nishibori, E.; Chiba, N.; Seong, G.; Tomai, T.; Adschiri, T. Fusion Growth and Extraordinary Distortion of Ultrasmall Metal Oxide Nanoparticles. *J Am Chem Soc* 2024, *146* (23), 16324–16331. <https://doi.org/10.1021/jacs.4c05106>.
  24. Yuan, Z.; Miao, H.; Jiang, Z.; Zhao, X.; Shi, S.; Zhu, X. Oxygen Vacancy Activated Inlaid Fe Active Sites in WO<sub>3</sub> for Sustainable and Efficient Photo-Fenton Oxidation in a Wide PH Range. *Molecular Catalysis* 2025, *577*. <https://doi.org/10.1016/j.mcat.2025.114962>.
  25. Yang, J.; Hao, J.; Wei, J.; Dai, J.; Li, Y. Visible-Light-Driven Selective Oxidation of Methane to Methanol on Amorphous FeOOH Coupled m-WO<sub>3</sub>. *Fuel* 2020, *266*. <https://doi.org/10.1016/j.fuel.2020.117104>.
  26. Yu, L.; Chen, J.; Liang, Z.; Xu, W.; Chen, L.; Ye, D. Degradation of Phenol Using Fe<sub>3</sub>O<sub>4</sub>-GO Nanocomposite as a Heterogeneous Photo-Fenton Catalyst. *Sep Purif Technol* 2016, *171*, 80–87. <https://doi.org/10.1016/j.seppur.2016.07.020>.
  27. Saleh, R.; Taufik, A. Degradation of Methylene Blue and Congo-Red Dyes Using Fenton, Photo-Fenton, Sono-Fenton, and Sonophoto-Fenton Methods in the Presence of Iron(II,III) Oxide/Zinc Oxide/Graphene (Fe<sub>3</sub>O<sub>4</sub>/ZnO/Graphene) Composites. *Sep Purif Technol* 2019, *210*, 563–573. <https://doi.org/10.1016/j.seppur.2018.08.030>.
  28. Wang, S.; Fan, W.; Liu, Z.; Yu, A.; Jiang, X. Advances on Tungsten Oxide Based Photochromic Materials: Strategies to Improve Their Photochromic Properties. *Journal of Materials Chemistry C*. Royal Society of Chemistry 2018, pp 191–212. <https://doi.org/10.1039/c7tc04189f>.
  29. Wei, J.; Jiao, X.; Wang, T.; Chen, D. The Fast and Reversible Intrinsic Photochromic Response of Hydrated Tungsten Oxide Nanosheets. *J Mater Chem C Mater* 2015, *3* (29), 7597–7603. <https://doi.org/10.1039/c5tc01350j>.
  30. Zeb, S.; Sun, G.; Nie, Y.; Xu, H.; Cui, Y.; Jiang, X. Advanced Developments in Nonstoichiometric Tungsten Oxides for Electrochromic Applications. *Materials Advances*. Royal Society of Chemistry November 7, 2021, pp 6839–6884. <https://doi.org/10.1039/d1ma00418b>.
  31. Wang, Z.; Einaga, H. WO<sub>3</sub>-Based Materials for Photocatalytic and Photoelectrocatalytic Selective Oxidation Reactions. *ChemCatChem*. John Wiley and Sons Inc November 8, 2023. <https://doi.org/10.1002/cctc.202300723>.





32. Lin, K.; Afzal, S.; Xu, L.; Ding, T.; Li, F.; Zhang, M. Heterogeneous Photo-Fenton Degradation of Acid Orange 7 Activated by Red Mud Biochar under Visible Light Irradiation. *Environmental Pollution* 2023, 327. <https://doi.org/10.1016/j.envpol.2023.121454>.
33. Sampaio, M. J.; Yu, Z.; Lopes, J. C.; Tavares, P. B.; Silva, C. G.; Liu, L.; Faria, J. L. Light-Driven Oxygen Evolution from Water Oxidation with Immobilised TiO<sub>2</sub> Engineered for High Performance. *Sci Rep* 2021, 11 (1). <https://doi.org/10.1038/s41598-021-99841-5>.
34. Zheng, J.; Gao, Z.; He, H.; Yang, S.; Sun, C. Efficient Degradation of Acid Orange 7 in Aqueous Solution by Iron Ore Tailing Fenton-like Process. *Chemosphere* 2016, 150, 40–48. <https://doi.org/10.1016/j.chemosphere.2016.02.001>.
35. Ke, J.; Zhou, H.; Liu, J.; Duan, X.; Zhang, H.; Liu, S.; Wang, S. Crystal Transformation of 2D Tungstic Acid H<sub>2</sub>WO<sub>4</sub> to WO<sub>3</sub> for Enhanced Photocatalytic Water Oxidation. *J Colloid Interface Sci* 2018, 514, 576–583. <https://doi.org/10.1016/j.jcis.2017.12.066>.
36. Huang, Z. F.; Song, J.; Pan, L.; Zhang, X.; Wang, L.; Zou, J. J. Tungsten Oxides for Photocatalysis, Electrochemistry, and Phototherapy. *Advanced Materials*. Wiley-VCH Verlag September 1, 2015, pp 5309–5327. <https://doi.org/10.1002/adma.201501217>.
37. Zhu, J.; Vasilopoulou, M.; Davazoglou, D.; Kennou, S.; Chroneos, A.; Schwingenschlög, U. Intrinsic Defects and H Doping in WO<sub>3</sub>. *Sci Rep* 2017, 7, 40882. <https://doi.org/10.1038/srep40882>.
38. Miyazaki, H.; Inada, M.; Suzuki, H.; Ota, T. Fabrication of WO<sub>3</sub>-Based Composite Films and Improvement Its Photochromic Properties by Copper Doping. *Bull Chem Soc Jpn* 2012, 85(9), 1053–1056. <https://doi.org/10.1246/bcsj.20120130>.
39. Miyazaki, H.; Inada, M.; Suzuki, H.; Ota, T. Molybdenum Doping Effects on Photochromic Properties of WO<sub>3</sub> Based Composite Films. *Journal of the Ceramic Society of Japan* 2013, 121 (1), 106–108.
40. Simchi, H.; McCandless, B. E.; Meng, T.; Shafarman, W. N. Structural, Optical, and Surface Properties of WO<sub>3</sub> Thin Films for Solar Cells. *J Alloys Compd* 2014, 617, 609–615. <https://doi.org/10.1016/j.jallcom.2014.08.047>.
41. Wei, J.; Jiao, X.; Wang, T.; Chen, D. The Fast and Reversible Intrinsic Photochromic Response of Hydrated Tungsten Oxide Nanosheets. *J Mater Chem C Mater* 2015, 3 (29), 7597–7603. <https://doi.org/10.1039/c5tc01350j>.
42. Santato, C.; Odziemkowski, M.; Ulmann, M.; Augustynski, J. Crystallographically Oriented Mesoporous WO<sub>3</sub> Films: Synthesis, Characterization, and Applications. *J Am Chem Soc* 2001, 123 (43), 10639–10649. <https://doi.org/10.1021/ja011315x>.
43. Yan, S.; Peng, C.; Yang, C.; Chen, Y.; Zhang, J.; Guan, A.; Lv, X.; Wang, H.; Wang, Z.; Sham, T. K.; Han, Q.; Zheng, G. Electron Localization and Lattice Strain Induced by Surface Lithium Doping Enable Ampere-Level Electrosynthesis of Formate from CO<sub>2</sub>. *Angewandte Chemie - International Edition* 2021, 60 (49), 25741–25745. <https://doi.org/10.1002/anie.202111351>.



44. Zinovieva, A. F.; Zinovyev, V. A.; Nenashev, A. V.; Kulik, L. V.; Dvurechenskii, A. V. Electron Spatial Localization Tuned by Strain in Ge/Si Quantum Dot Heterostructures. *Phys Rev B* 2019, *99* (11). <https://doi.org/10.1103/PhysRevB.99.115314>.



- The data supporting this article have been included as part of the Supplementary Information.

